Surface reactivity and surface characterization of the layered β(III)-CoOOH material: an experimental and computational study

Alexia Lemoine, Ronan Invernizzi, Germain Vallverdu, Lénaïc Madec, Jacob Olchowka, Liliane Guerlou-Demourgues, Isabelle Baraille, Delphine Flahaut

Surface Reactivity and Surface Characterization of Layered β(III)-CoOOH Material an Experimental and Computational Study

Alexia Lemoine[1], Ronan Invernizzi[2,3], Germain Salvato Vallverdu[1,3*], Lénaïc Madec[1,3], Jacob Olchowka[2,3,4], Liliane Guerlou-Demourgues[2,3,4*], Isabelle Baraille[1,3], Delphine Flahaut[1,3]

[1]   Université de Pau et des Pays de l'Adour, E2S UPPA, CNRS, Institut des Sciences Analytiques et de Physico-chimie pour l'Environnement et les Matériaux, UMR 5254, 64000 Pau, France

[2]   CNRS, Univ. Bordeaux, Bordeaux INP, ICMCB UMR 5026, F-33600 Pessac, France

[3]   RS2E, Réseau Français sur le Stockage Electrochimique de l'Energie, FR CNRS 3459, F-80039 Amiens Cedex 1, France

[4]   ALISTORE-ERI European Research Institute, FR CNRS #3104, Amiens, F-80039 Cedex 1, France.

Corresponding authors

* germain.vallverdu@univ-pau.fr +33 5 59 40 78 51

* liliane.guerlou-demourgues@enscbp.fr +33 5 40 00 27 25

Abstract

In this article we focused on the comprehension of the surface reactivity of layered β(III)-cobalt oxyhydroxide, β(III)-CoOOH, by implementing a multi-scale study associating both experimental, surface characterization by X-ray Photoemission Spectroscopy (XPS) and microscopy (SEM) and first-principle calculations. The surface reactivity and the chemical properties of the surface are key factors in the charge storage mechanism and β(III)-CoOOH presents interesting characteristics to be used as pseudo-capacitive electrode materials in supercapacitors thanks to its large surface specific area (~100 $m^2.g^{-1}$) and its high electronic conductivity (10^{-3} to 1 $S.cm^{-1}$). The surface reactivity (basic and redox character) of the synthesized compounds, which consists in aggregates of particles with 60-

100 nm length, has been explored from the adsorption of SO_2 molecules followed by XPS analyses. A kinetic study of the reactivity allowed us to identify three steps in the adsorption mechanism of our β(III)-CoOOH samples. The coupling of XPS and computational results allows us to establish a link between the surface reactivity in the identified domains, the formation of sulfate and sulfite species, and the cobalt Co^{3+} and Co^{4+} species of the active sites along with the underlying electronic processes.

KEYWORDS: Surface Reactivity; First-Principle Calculations; Supercapacitors; Energy Storage, reaction mechanism

I) Introduction

Supercapacitors are energy storage devices that rely on fast surface/interface reactions of the electrodes materials to store the charges, which make them ideal candidates for high power applications.[1] In EDLCs (electric double layer capacitors), the predominant capacitive storage mechanism that consists in adsorption/desorption of ions from the electrolyte on the carbon electrodes surface, is limited by the specific surface area, resulting in restrained energy densities. Thus, compared to Li-ion batteries (LIB), the energy density delivered by commercial EDLC (3-10 Wh/kg vs. ~250 Wh/kg for LIB) can be a drag to portable applications where high autonomy is required. [2,3] To increase the energy density of supercapacitors, a possible way is to replace one of the two carbon electrodes by a pseudo-capacitive or a battery electrode to build pseudo-capacitors and hybrid capacitors respectively.[4, 5, 6]

The charge storage mechanism of pseudo-capacitive materials, which is based on rapid and reversible redox reactions (Faradaic process) at the surface/near surface of the active material, allows increasing energy densities without compromise on the high power, whereas the diffusion-limited process in battery electrode hampers the power response.[6, 7] Thus, the characteristics of pseudo-capacitors appear to be very attractive for the next generation of energy storage devices. In the literature, different oxides and oxyhydroxides such as RuO_2, MnO_2, $FeWO_4$ or CoOOH, and more

recently MXene, have been reported to exhibit rectangular shape cyclic voltammograms in aqueous electrolyte, characteristic of pseudo-capacitive materials.[8-12] As only the surface is used in the charge storage mechanism, the nano-structuration of the pseudo-capacitive materials is essential to optimize the electrochemical performance. Moreover, the nanoscale design improves the electrolyte accessibility to the material particles surface and favours the ionic diffusion through the electrode material. However, increasing the specific surface area (SSA) does not necessary improve the capacitance since the surface reactivity for a given material differs depending on, among others things, the crystallographic planes and the eventual presence and accessibility of redox active sites. For instance, it is reported that CoOOH functionalized with $BMIMBF_4$ ionic liquid exhibits a higher pseudo-capacitive response than pristine CoOOH although its specific surface area is lower.[12] Understanding the surface reactivity of the pseudo-capacitive materials is thus a key point to develop a rational strategy and reach the best energy storage performance. To this end, we followed a strategy previously used in our group on the investigation of lithium-ion battery electrode materials that allowed us to get a deep insight on the chemical properties of the surface and the electronic processes taking place[13-15]. This strategy aims to probe the surface reactivity from a combined experimental and computational investigations including: synthesis, surface characterization before and after gas probe adsorption and first-principle calculations.

In this work, a focus is made on the layered β(III)-cobalt oxyhydroxide phase ($H^+_wNa^+_yCo^{x+}O_2.n(H_2O)$)) which possesses interesting characteristics for pseudo-capacitive electrode materials. Indeed, depending on the stoichiometry of H, which is linked to the amount of Co^{4+}, this material has an excellent electronic conductivity (10^{-3} up to 1 $S.cm^{-1}$) compared to most of other pseudo-capacitive oxides and hydroxides, good stability in aqueous electrolyte and can easily be synthesized as nanocrystalline powder with SSA higher than 100 m²/g.[16-19] However, the experimental pseudo-capacitive response of β(III)-cobalt oxyhydroxide, far below the theoretical expectation, leads us to perform a multi-scale study to investigate in details the reactivity of the different surfaces, the

nature of the active sites and to identify the mechanisms involved in the charges storage.[8, 12] To do this, the adsorption of gas such as SO_2 was carried out to probe the nature of the active sites. X-ray photoelectron spectroscopy (XPS) was used to characterize the surface in terms of electronic structure and composition of the material and also to determine the adsorption mode of SO_2 (redox and / or acid/base). Scanning Electron Microscopy (SEM) was used to highlight the morphology of β(III)-cobalt oxyhydroxide. Theoretical calculations were made to study, at the atomic scale, the surface and bulk properties as well as the adsorption mechanisms.

II) Materials and methods

1) Synthesis and bulk characterization of β(III)-CoOOH

For the synthesis of β(III)-CoOOH, 3.18 g of $Co(NO_3)_2.6H_2O$ (10^{-2} mol) were dissolved in 300 mL of distilled water. The solution of cobalt nitrate was added dropwise into 11 mL of NaOH (2M) under stirring, forming an unstable blue precipitate corresponding to $Co(OH)_2$, xH_2O (α hydrated variety). After few seconds, this precipitate has turned pink, leading to the formation of $Co(OH)_2$ (β(II) unhydrated variety). Then, 7.5 mL of NaClO (48° Cl) was added dropwise to the solution in order to speed up the oxidation process leading to the oxyhydroxide phase. The solution was stirred during 30 minutes, centrifuged few times in distilled water for 5 min at 4000 rpm until neutral pH and dried 24 h at 40 °C.

XRD analyses A Philips Panalytical X'Pert Pro diffractometer was used to record X-ray powder diffraction patterns. Co-K_α radiation ($\lambda_{K\alpha2}$= 1.7928 Å, $\lambda_{K\alpha1}$= 1.7889 Å) was used in order to avoid fluorescence, problematic with traditional Copper sources, and to generate high quality patterns. The powder diffraction patterns were recorded for about 16 h in the 20°−90° (2θ) angular range, with a 0.02° (2θ) step size and a 2.022° (2θ) active width in the detector.

ICP-OES Co and Na elements were quantified in our samples using a Varian 720ES ICP-OES spectrometer. The samples were prepared by dissolving 25 mg of powder into HCl, the solutions being heated until full dissolution of powder. Then the solutions were diluted in order to obtain a concentration of target element between 1 and 200 mg/L. The solution was then introduced in a nebulization chamber along with an argon flow to create an aerosol. Five measurements were realized for each sample for accuracy.

CHNS To quantify the % of hydrogen in the sample, 1.5 mg of the sample was burned at 920 °C in a tin foil in an excess of oxygen. The combustion products were collected (H_2O) and quantified thanks to a Thermo Flash EA 111E Series apparatus. Two measurements were conducted for each sample to control the accuracy.

IODOMETRIC TITRATION Mean oxidation states of Co were determined by iodometric titration. Around 25-30 mg of powder are dissolved in 5mL of distilled water, 10 mL of KI solution at 10 g/L and 5 mL of 12MHCl solution. The solution was heated until total dissolution of powder (yellow color). Immediately after, the solution was titrated by sodium thiosulfate in order to obtain V_{eq} when the solution turns for yellow to pink.

The I^- ions (KI) reduce all the cobalt ions to the divalent state.

This reaction leads to the oxidation of I^- ions and to release I_2.

$$(x-2)I^- + Co^{x+} => Co^{2+} + \frac{x-2}{2}I_2$$
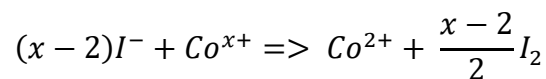
The I_2 molecules are then titrated by sodium thiosulfate (0.1 M $Na_2S_2O_3$):

$$2\,(S_2O_3)^{2-} + I_2 \rightarrow S_4O_6^{\,2-} + 2I^-$$
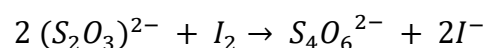
To calculate the mean oxidation state of cobalt, the quantity of I_2 formed can be expressed as:

$$n_{I_2} = \frac{x-2}{2}nCo^{X+} = \frac{1}{2}\left[S_2O_3^{\,2-}\right] * Veq$$

where V_{eq} is the volume of sodium thiosulfate added at the equivalence. It is therefore possible to determine x:

$$x = \frac{[S_2O_3{}^{2-}] * Veq}{nCo^{X+}} + 2$$

The following methodology is used to establish a chemical formula of the material such as $H^+{}_wNa^+{}_yCo^{x+}O_2.n(H_2O)$: once the concentrations of Na, Co (ICP-OES) and H (CHNS) are determined, the molar ratio of each element to Co is calculated. The proton amount (w) is deduced by considering the total charge neutrality, and the amount of water molecules is obtained by subtracting the proton amount from the total H element amount.

2) Surface analysis

X-ray Photoelectron Spectroscopy (XPS) XPS analysis were performed on a Thermo K-alpha spectrometer using a focused monochromatized Al Kα radiation (hν = 1486.6 eV). The analysis depth is 5 nm and the analysis area represents an ellipse of 200 x 400 μm^2. A Cu double tape was used to fix the powder on the sample holder. In order to avoid any contamination and air contact after SO_2 adsorption, the samples were prepared in a glove box and transferred into the glove box which is directly connected to the spectrometer ($H_2O/O_2 < 5$ ppm) using a transfer vessel. The core peaks were recorded with a pass energy of 20 eV and an energy step of 0.1 eV. Neutralizer gun, which sprays low energy electrons over the sample surface to minimize the surface charging, was employed for charge compensation. XPS spectra processing and quantification was obtained using CASA XPS software after Shirley-type background subtraction. Quantification of surface composition was based on Scofield's relative sensitivity factors.[20]

Scanning electron microscopy (SEM) An Auger JEOL JAMP 9500F spectrometer was used for Scanning electron microscopy (SEM).

In order to analyze both the surface and the core of the bare material, samples were cut with a JEOL IB-09010CP cross polisher under a controlled atmosphere of nitrogen in a glove box. For this, the β(III)-CoOOH powder was mixed with isopropanol-carbon to ensure a low charge effect and then deposited on a silicon wafer. The wafer as well as the powder-matrix carbon mixture was then cut with Argon plasma of 6 kV and 150 μA. The cutting depth of the sample is about 100 μm.

The cut sample was then directly transferred from the glove box to the Auger spectrometer for analysis using a transfer vessel.

The SEM images highlighting the morphology of β(III)-CoOOH were carried out under Ultra High Vacuum conditions ($<2x10^{-7}$Pa). An acceleration voltage of 20 kV and a current beam of 4 nA has been used.

Specific area The specific surface area of the β(III)-CoOOH material was determined using Micromeritic ASAP 2010 and with the Brunauer-Emmett-Teller (BET) theory. For this, a gas adsorption of N_2 was carried out at a temperature of 77.300 K.

3) Gas probe adsorption

The SO_2 adsorption was carried out with a Micromeritics Autochem 2920 Analyzer in four steps: (i) the reactor was cleaned by heating at 500°C for 1 h under argon flow, (ii) the β(III)-CoOOH powder (m = 0.050 g) was introduced in this reactor and was cleaned of adsorbed species under argon flow at 80°C for 1 h, (iii) the adsorption of SO_2 was performed under helium flux containing 1000 ppm of SO_2 with a flow of 50 mL.min^{-1}. The adsorption has been maintained for: 5, 15, 30, 45 and 60 minutes, (iv) finally, a desorption step of physisorbed species has been conducted at 80°C under helium flow for 1 h.

Each series of samples was investigated three times in order to check the reproducibility of the adsorption mechanism. After adsorption, β(III)-CoOOH powder is stored in a glove box under

controlled atmosphere until it is analyzed. The SO_2 desorption is monitored as a function of time (see supporting information Figure SI-1) and the maximum storage time of the sample in the glove box between adsorption and XPS analysis can be set at one week to avoid any SO_2 desorption.

SO_2 gaseous probe was chosen because sulfur is not present in the material and also exhibits a large B.E. scale. The adsorption of gas probes, such as SO_2, makes it possible to determine both the nature and the concentration of the active sites on the surface[21-22], either acid-base or redox engaged in redox surface reactions, associated to faradaic process, and electrostatic adsorption associated to capacitive storage. Indeed, if SO_2 molecules are adsorbed on the surface in sulfite species (SO_3^{2-}), the active sites are basic. On the other hand, if SO_2 molecules are adsorbed in sulfate species (SO_4^{2-}), the active sites are oxidizing. The content of adsorbed species is determined from XPS analysis through the area ratio between the S 2p and the Co 2p core peaks. The adsorption mode is assigned depending on the S 2p core peak binding energy. A binding energy (B.E.) of the S $2p_{3/2}$ core peak at 167.5 eV is characteristic of sulfite species and the formation of sulfate species is characterized by a B.E. of 169.0 eV[21, 22]. Due to the ultra-high vacuum conditions of XPS analyses, only the chemisorbed species are detected as the interactions involved in physisorption are too weak.

4) Theoretical calculation

All calculations were performed using the plane wave density functional theory (DFT) approximation available in the Vienna Ab Initio Simulation Package (VASP)[23, 24]. The electronic wave-functions were described in the Projected Augmented Wave (PAW) formalism[25] using a spin polarized electronic density within the generalized gradient approximation, using the Perdew-Wang-Ernzerhof (PBE) functional[26]. An energy cutoff of 500 eV was used to define the plane wave basis set and the Brillouin zone integration was sampled using 8×8×2 and 2×2×1 k-points grids for bulk and slab calculations respectively. To account for the strongly localized character of 3d-electrons of cobalt atoms, DFT+U calculations were implemented using a Hubbard correction in the framework of the rotationally

invariant approximation of Dudarev *et al.* [28]. According to previous works on cobalt oxides[29,35,36] we performed DFT+U calculations with U = 3.3 eV.

β(III)-CoOOH exhibits a hexagonal structure and crystallizes in a $R\bar{3}m$ space group with lattice parameters a = b = 2.84 Å and c = 13.16 Å [30]. After a full relaxation of the system (shape, volume and ions positions), optimized lattice parameters are a = b = 2.874 Å and c = 13.027 Å, the shape of the cell being unchanged. The deviation of the computed lattice parameters from the experimental ones is less than 1%. (see Table SI-2). The computed density of states (DOS) of the bulk agrees with the XPS valence band, which enforces the accuracy of our computation level and Hubbard correction, see Figure SI-2.

In this work, we considered the low index (001), (110), (012), (015) and (101) crystalline surfaces represented using slab models. These slab models were built from the optimized bulk structure and consisted in the stacking of several atomic layers perpendicularly to the considered surface plane. A vacuum volume of 15 Å height was left free in the direction perpendicular to the surface plane to quench spurious interaction between periodic images. The thickness of the slabs was chosen such as bulk properties were obtained at the central atomic layers. Some of these slabs correspond to polar surfaces of tasker type 3[32]. To avoid the formation of any electrostatic dipole, all slabs are built to be symmetric either from a center of symmetry or a mirror plane at the center of the cell. A full description of the five slabs, Figure SI-8, is available in supporting information. All the atomic positions were relaxed except for the atoms of the central layer to avoid slab translations in the unit cell. All cobalt atoms surrounded by six oxygen atoms in an octahedral geometry, as in the bulk, were considered to be in a low spin state $(t_{2g})^6(e_g)^0$. The spin states of under-coordinated cobalt atoms were explored by probing different electronic configuration, keeping a ferromagnetic ordering between atoms.

The surface formation energies were calculated from the following equation

$$E_{surf}^{hkl} = \frac{1}{2S}\left(E_{slab}^{hkl} - nE_{bulk}\right)$$

where E_{surf}^{hkl} and E_{bulk} correspond to the energies of the optimized slab and bulk energies respectively. S is the area of the surface of the slab and *n* the number of bulk formula unit in the slab model.

SO$_2$ adsorption was done on top of the slab models. The formation of sulfite and sulfate species corresponds to top and bridge adsorption sites, respectively. The adsorption energies were computed from

$$E_{ads} = E_{slab+SO_2}^{hkl} - E_{slab}^{hkl} - E_{SO_2}$$

where $E_{slab+SO_2}^{hkl}$ corresponds to the energy of the slab with one SO$_2$ molecule adsorbed on the top atomic layer and E_{SO_2} is the energy of an isolated SO$_2$ molecule. This energy was computed by isolating a SO$_2$ molecule in a cubic box of 10 Å length.

The Bader decomposition of the charge and spin densities was performed using a finer grid for the electronic density around 0.03Å [33, 34]. The difference between the number of α and β electrons (n$_\alpha$ - n$_\beta$) is reported as magnetic moment and labeled μ. These quantities are valuable probe of the oxidation degrees of transition metal atoms. Calculations of atomic charges and magnetic moments were performed on an ensemble of benchmark cobalt oxide structures and are used as reference to discuss the results obtained on slab systems. The computational details and the results of these calculations are reported in the supporting information section II.[38]

III) Results and discussions

A) <u>β(III)-CoOOH material before SO$_2$ adsorption</u>

    1) <u>Crystallographic structure</u>

The X-Ray diffraction pattern presented in Figure 1 confirms that the synthesis leads to the formation of pure rhombohedral CoOOH phase. All the reflections can be indexed in a hexagonal cell, with 3 CoO$_2$ slabs per cell leading to $R\overline{3}m$ space group and cell parameters: a = b = 2.84 Å and c = 13.16 Å.[31] The broad reflections reveal small coherent domains of ~ 30 nm and ~10 nm, calculated using Scherrer equation on (003) and (110) reflections.[38]
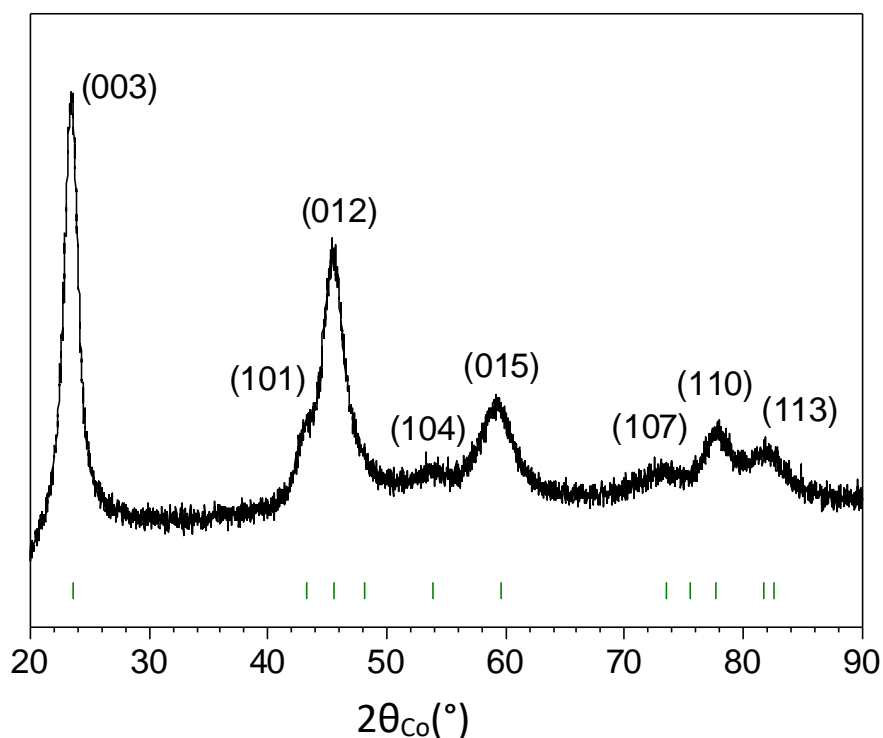
Figure 1: X-ray diffraction pattern of the synthesized β(III)-CoOOH phase. Green ticks are the positions of reference peaks of ICSD-22285.

As detailed in the experimental part, the exact chemical composition of the cobalt oxyhydroxide was determined on the basis of the H/Co, Na/Co ratio (ICP-OES and CHNS data) and the average oxidation state of cobalt (iodometric titration). These data, which are gathered in Table 1, lead to the following chemical formula for the material: $H_{0.84}^{+}Na_{0.06}^{+}(H_2O)_{0.19}Co^{3.10+}O_2$. However, for practical reasons, the material will be denoted as "CoOOH" all along the manuscript.

Table 1 – Chemical composition of the synthesized CoOOH phase

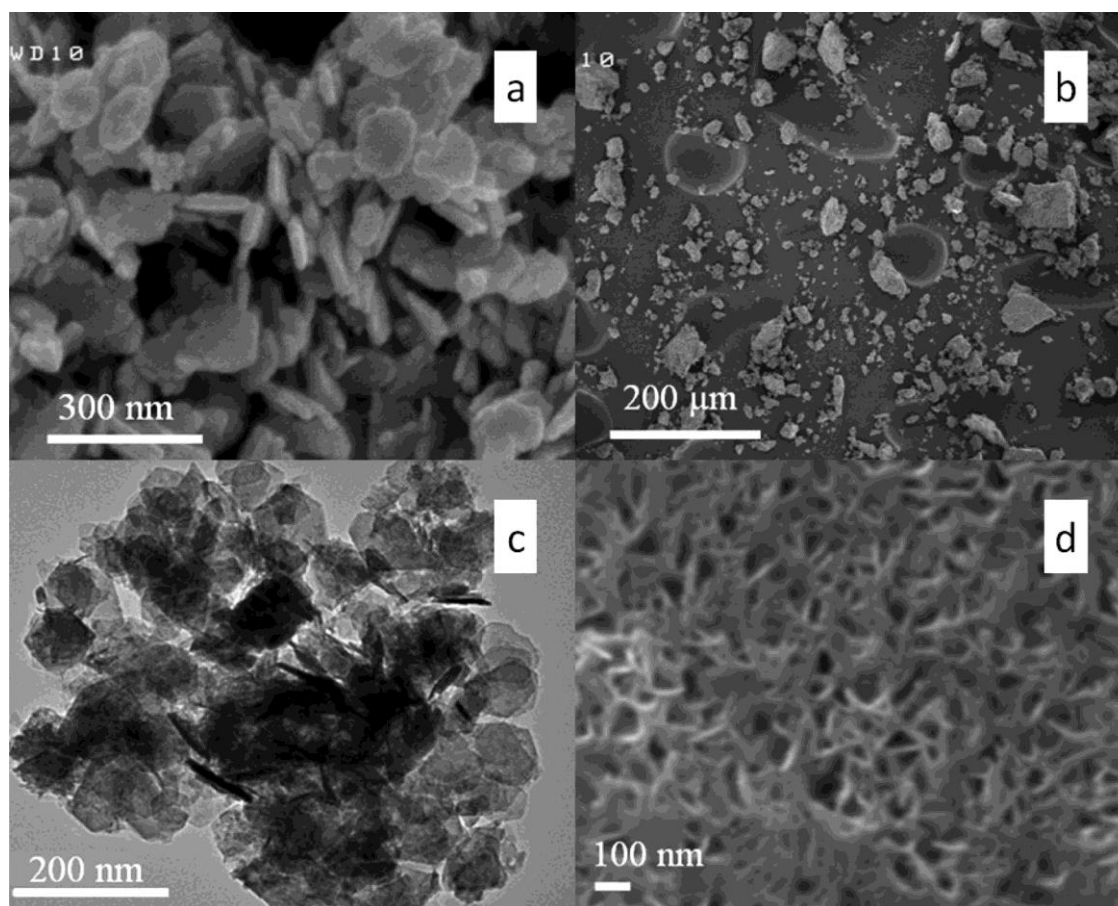| Sample	Atomic ratios		Mean oxidation state of Co	Chemical formula
	H/Co	Na/Co		
ß(III)-CoOOH	1.22	0.06	3.10	$H_{0.84}^{+}Na_{0.06}^{+}(H_2O)_{0.19}Co^{3.10+}O_2$

2) <u>Morphology</u>

Figure 2: a) and b) SEM images, c) TEM images and d) cross section SEM image of the β(III)-CoOOH sample

Figure 2 reports the SEM and TEM images obtained on uncut samples (Figure 2.a), 2.b) and 2.c)) and cut sample with the cross polisher of β(III)-CoOOH (Figure 2.d)). The β(III)-CoOOH material consists of well-defined hexagonal platelets of about 60 to 100 nm length and 10 nm thickness.[8,16,39] The low thickness of those particles corresponds to the coherent domain size, whereas the length coincides with 2 or 3 crystallites merged together. The platelets coalesce to form aggregates of various sizes, from few to several tens of micrometers (Figure 2.a) et 2.b)). On the figure 2.d), SEM image of the cut sample provides information on the core of the agglomerates. The particles are randomly organized and the material exhibits a very high porosity with the presence of many channels within the aggregates. The surface area of this material was estimated at about 110 m^2/g and is in the same order as for other CoOOH reported in the literature (between 55 m²/g and 241 m²/g).[12, 19, 40,41] This surface area is intermediate between the values obtained for materials used in batteries like $LiCoO_2$ (up to 50 m^2/g)[42] and for carbon-based materials used in supercapacitors (~ 1000-3000 m^2/g)[43,44]. The synthesis method used in this work allows thus to obtain nanostructured CoOOH material with a large SSA, which is a key parameter to obtain good performances. Indeed, the electrolyte accessibility to the material surface, where the reactions engaged in the charge storage mechanism take place, is governed by the material morphology.

3) <u>Surface characterization</u>

The survey spectra of all samples are displayed in Figure SI-3. The materials surface contains Cobalt, Oxygen, Carbon (contamination) and Sodium (synthesis residue) elements. Sulfur is detected after adsorption.
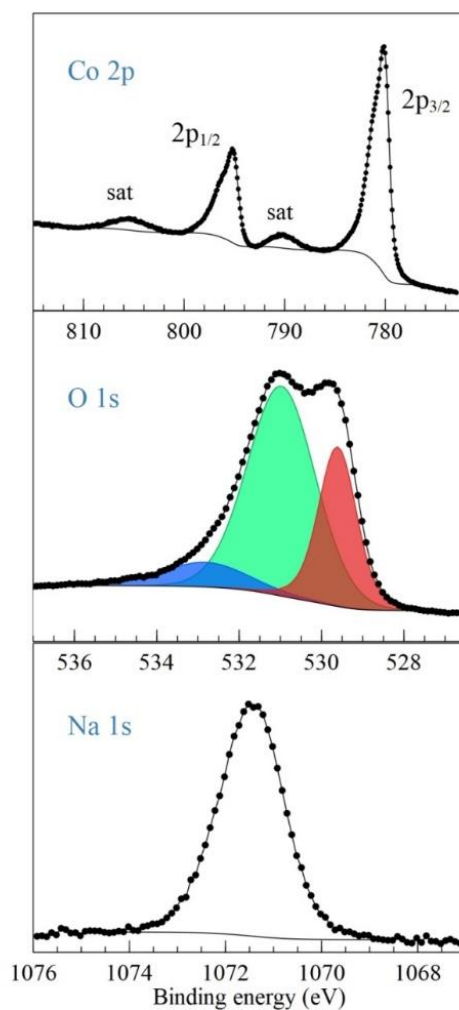
Figure 3: Co 2p, O 1s (red : oxide anion, green : adsorbed and bulk hydroxide and under coordinated oxide ; blue : water and adsorbed species) and Na 1s core peaks spectra of the bare β(III)-CoOOH material

All the spectra presented in this work were calibrated in the C 1s scale from the adventitious carbon at 285.0 eV. The XPS spectra of Co 2p, O 1s and Na 1s of the bare β(III)-CoOOH compounds are shown in Figure 3.

For the Co 2p spectrum, two peaks are observed due to the spin-orbit coupling: the first at 780.3 eV corresponds to $Co\ 2p_{3/2}$ (with a FWHM of 2.3eV) and the second at 795.0 eV corresponds to $Co\ 2p_{1/2}$. There are also 2 satellite peaks located at 790.3 eV and 805 eV, with area corresponding to 7% of the associated main peaks $Co\ 2p_{3/2}$ and $Co\ 2p_{1/2}$. As previously reported in the literature[30],

the binding energy of the satellite peaks is efficient to estimate the presence of the Co^{+2} or $Co^{+3/+4}$ in oxide materials especially. The B.E. of the core and the satellite peaks confirm, here, the predominant presence of Co^{3+} on the material surface without exclude a contribution of Co^{+4}. The Co^{2+} species can be excluded as no satellite peak has been detected at 786 eV and 803 eV.[45, 46] To get deeper in the determination of the cobalt valence, the signature of the Co 3s spectra have been checked. In the work of Daheron *et al.*[30], it is obvious that the cobalt valency can be easily identify by considering the Co 3s core peaks. The Co 3s spectra of our samples are reported in Figure SI-4b. The envelopes of the spectra are identical before and after adsorption, and close to the envelope of the $LiCoO_2$ compound. Moreover, the main component is located at 103.0 eV and the FWHM is 3.2 eV, confirming that the Co^{+3} contributes in a major part to the signal[30]. The slight enlargement of the peak is the signature of a slight content of Co^{+4}, which is consistent with the 1-6% of Co^{+4} determined from Co 2p spectra.

According to reference 30, we can roughly estimate the Co^{+4} content in our samples. Dahéron *et al.* have reported that the satellite area for a pure Co^{3+} in $LiCoO_2$ is of 9.1%. Upon lithium deintercalation in $Li_{1-x}CoO_2$, the amount of Co^{4+} species increases and the satellite area decreases concomitantly with the enlargement (FWHM) of the Co 2p core peaks to reach, respectively, 4.6% and 3.2 eV for the CoO_2 material composition. Therefore, these two criteria can be a tool to determine the range of Co^{+4} content. The fine decomposition of the Co 2p spectrum of the βIII-CoOOH sample before adsorption provides a satellite relative area of ~ 7% and a FWHM of 2 eV for the Co 2p$_{3/2}$ main peak. Thus, from the Table 1 of the ref 30, we estimate that the cobalt valency is between the valency of $Li_{0.99}Co^{+3.01}O_2$ and $Li_{0.94}Co^{+3.06}O_2$. We thus determine that our material contains roughly 1-6% of Co^{4+}.This result is consistent with the results obtained by iodometric titration showing an average oxidation state for cobalt of +3.1 (approximately 10% of Co^{4+}).

The O 1s spectrum can be decomposed into three components at 529.5 eV, 531.2 eV and 533.0 eV. The component at 529.5 eV is assigned to the bulk O^{2-}, referring to the oxide part of the material. According to the chemical formula $H_{0.84}Na_{0.06}CoO_2, 0.19\,H_2O$, the OH and O^{2-} environments in the

bulk should be equivalent with a nominal ratio Co:O of 1:2. However, the Co: O^{2-} ratio is 1:0.94 while the Co:$O_{531.2ev}$ ratio is 1:2.21. Thus, the O 1s component at 531.2 eV can be attributed to the hydroxyl groups located in the bulk as well as to adsorbed OH and potentially under coordinated surface oxygen atoms at the surface of aggregates. The last component at 533.0 eV corresponds to the presence of water and adsorbed species. These attributions of the different components agree with the results of previous studies carried out on cobalt oxyhydroxide.[27,31,37]

The detection of Na in the sample is due to the presence of a few sodium atoms between the nanosheets and also to the synthesis conditions (see experimental part).

4) Surfaces

Electronic structure calculations were implemented to deepen the knowledge of the electronic properties of the bare surfaces and complete the experimental results. As reported in Table SI-2 in supporting information, for the β(III)-CoOOH relaxed bulk structure, the Co-O bond length is 1.92 Å, the atomic charge of the cobalt atom is 1.31e and the most stable spin state is the low spin state with no magnetic properties due to a $(t2g)^6(eg)^0$ configuration. We considered the (001), (110), (012), (015) and (101) crystalline surfaces, which correspond to the more intense peaks on the XRD diagram, and built slab models associated to each surface. The computed surface formation energies are gathered in Table 2. The structural data of the slabs are presented in the supporting information Table SI-3. Figure 4 presents the side views of the (001), (110) and (012) slab models along with the electronic configuration of cobalt atom in the central and the top cobalt atomic layer. The same representations are available in the supporting information (Figure SI-8) for slab models (015) and (101).

The lowest surface formation energy is obtained for the (001) slab model, which corresponds to the plane perpendicular to the stacking direction of β(III)-CoOOH sheets in the bulk. In this slab, Figure 4 a), the cobalt atoms are in the same ML_6 environment as the bulk. All cobalt atoms of the slab exhibit the same electronic and geometric characteristics as those of the bulk. For the (001) slab, the Co-O

bond lengths are 1.92 Å and the cobalt atoms exhibit a charge of 1.32e and a zero magnetic moment associated to the low spin state of a Co^{3+} species.

Table 2: Surface formation energies, E_{surf}^{hkl}, computed from the slab models in J.m^{-2}.

Slab	E_{surf}^{hkl} (J.m^{-2})
(001)	0.593
(110)	0.784
(012)	1.33
(015)	2.40
(101)	2.88

The formation of the (012) surface leads to the loss of one Co-O bond and thus cobalt atoms on the top surface layer are in a ML$_5$ environment, Figure 4b). The length of the Co-O bond roughly perpendicular to the surface plane is 2.02 Å, longer than the bulk one, while the other four Co-O bond lengths are 1.90 Å, as in the bulk. This environment leads to a degeneracy break of the e$_g$ orbitals and the cobalt atoms exhibit a magnetic moment of 1.94 µ$_B$ associated with an electronic charge of 1.32e. According to the reference calculations, see Figure SI-11 in supporting information, these results correspond to a Co^{3+} species in an intermediary spin configuration as depicted in Figure 4 b. For the (015) and (101) slab models, the cobalt atoms on the top atomic layer are also in a ML$_5$ environment with atomic charges of 1.39e and 1.35e and magnetic moments of 2.01 and 1.97 µ$_B$, respectively. These results also correspond to Co^{3+} species as already observed for the (012) slab model. In the following, the ML$_5$ environment of Co with a degree of oxidation +III will be represented by the (012) slab model as it corresponds to the most stable surface compared to (015) and (101) slab models. The cleavage of the bulk along the (110) surface leads to the break of two Co-O bonds and cobalt atoms on the top surface layer are thus in a ML$_4$ environment, as shown in Figure 4 c. The length of the two Co-O bonds

in the surface plane is 1.81 Å while the length of the two remaining bonds is 1.96 Å. The cobalt atoms of the top surface layer exhibit a magnetic moment of 2.95 μ_B, along with a charge of 1.43e, higher than the bulk one. According to the reference calculations, see Figure SI-10 in supporting information, these results agree with a Co^{4+} species in an intermediary spin state as shown in Figure 4 c. The presence of these Co^{4+} species agree with the observation from XPS characterization (Figure 3).
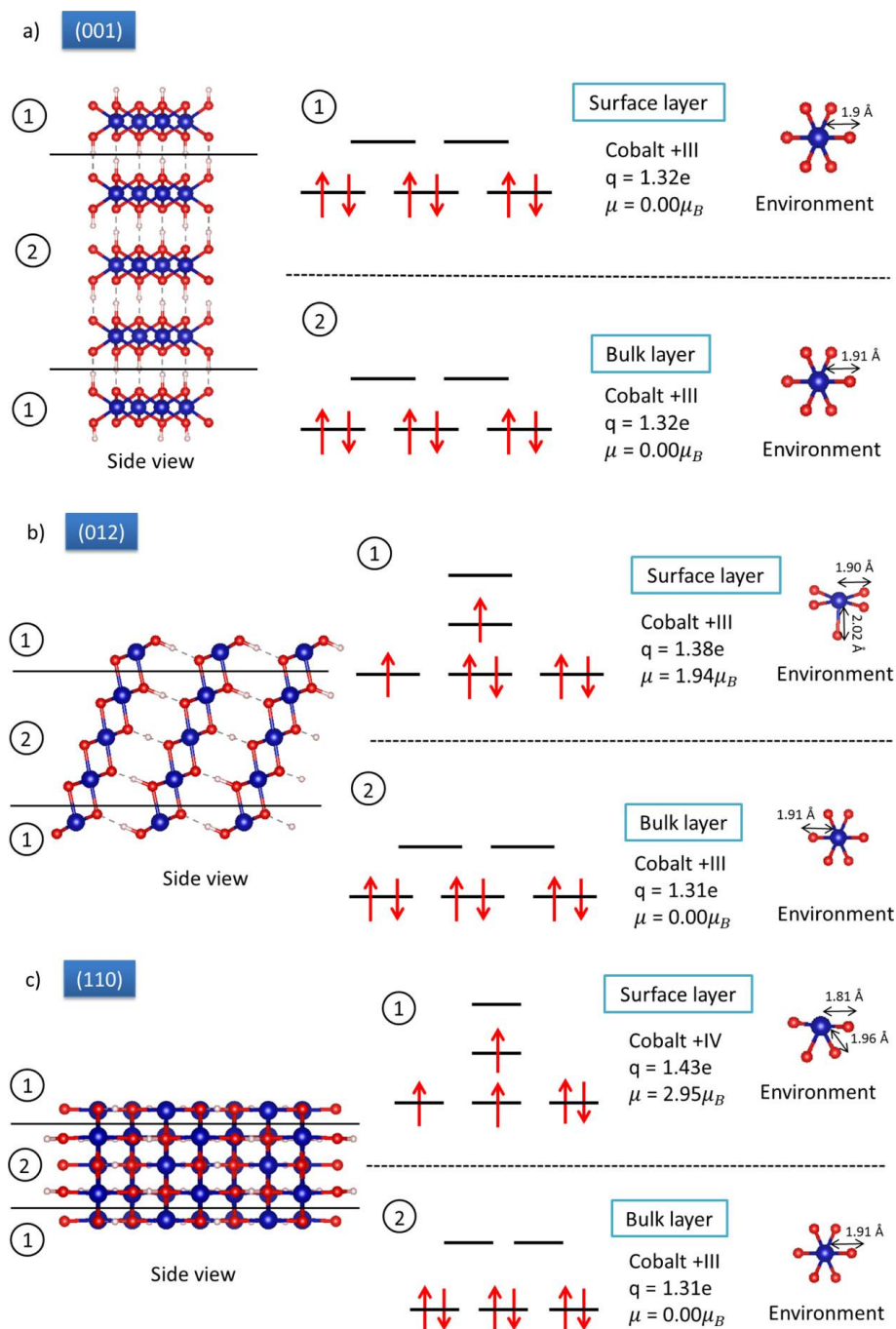
Figure 4: a) slab (001) and the electronic configuration of Co, b) slab (012) and the electronic

configuration of Co, c) slab (110) and the electronic configuration of Co for (βIII)-CoOOH.

In conclusion of these results on the bare material, both experimental (XPS and ICP/iodometric titration) and computational methods demonstrate that β(III)-CoOOH can be described as a material with a cobalt mixed oxidation state containing a major proportion of Co^{3+} and a minor proportion of Co^{4+} (1-6%). The theoretical calculations on the slab models specify the conditions of the presence of Co^{4+} that plays a crucial role in the final properties of this material. In particular, it is known that the Co^{4+} species are responsible for the good electronic conductivity of the material.[17,47-49]

In the following, we will focus on the (001), (110) and (012) surfaces. These three slab models correspond to the most stable surfaces and allow us to consider three different cobalt environments on the top atomic layer, namely ML_4, ML_5 and ML_6. These chemical environments may be associated to the available reactive sites on the surface of the β(III)-CoOOH material.

B) β(III)-CoOOH material after SO_2 adsorption

1) *Surface investigation*

The purpose of subjecting the material to a SO_2 gas flux was to determine the nature and the concentration of the active sites on the surface. A follow-up of the S/Co ratio (Figure 5.a.) as a function of the exposure time (5, 15, 30, 45 and 60 min) to the SO_2 gas flow was carried out by XPS analysis from the S 2p (Figure 5.b) and Co 2p (supporting information S3) core peaks. The quantifications extracted from XPS analyses are available in the supporting information (Table SI-1).

The Co 2p core peak spectra remain unchanged for any SO_2 exposure time, which means that there are no detectable changes in the oxidation state of cobalt upon the adsorption. (see supporting information Figure SI-4a)

Figure 5.a reports the evolution of the adsorbed species content as a function of the SO_2 exposure time by checking the S / Co at. % ratio. Three steps can be identified according to the noticeable slope changes. In step 1, the S/Co ratio values increase rapidly up to an exposure time of 15 min. The SO_2 gaseous probes are gradually adsorbed on the surface of the aggregates. Then (step 2), from 15 min to 30 min of exposure time, no more SO_2 is adsorbed on the surface samples, which corresponds to the saturation of the sample surface. The nature of the adsorbed species has been determined according to the S 2p spectra. They exhibit a main doublet and a minor one, with S $2p_{3/2}$ component located respectively at 166.9 eV and 168.7 eV, assigned to the sulfite and sulfate species. The sulfate species associated to redox adsorption mechanism represent 90% of the whole surface active sites. The oxygen atoms from adsorbed SO_2 molecules lead to an increase of O 1s component located at 531.1 eV (see supporting information Figure SI-5). Beyond 30 min (step 3), the S/Co ratio values rise again. The main adsorption mode is still redox (B.E. S $2p_{3/2}$ = 168.7 eV) with a small contribution of the acid-base mechanism (B.E. S $2p_{3/2}$ = 166.9 eV) linked with the detection of sulfite species. A third doublet is also appearing on the S2p spectra at B.E. S $2p_{3/2}$ = 170.5eV (see Figure 5.b).

From figure 5.a, we understand that the whole available active sites (basic and redox) located on the aggregates surface have reacted with the SO_2 gaseous probes (step 2). And, after reaching a pseudo equilibrium, the SO_2 chemisorption continues with the detection of a third sulfur specie. To explain this phenomenon, note that samples revealed the presence of channels induced by platelets disorganization with each other (Figure 2. d). A schematic view of the location of the SO_2 adsorption in the three zones is presented in Figure 6. Since the active sites located on the aggregates surface have been saturated by SO_2 chemisorption, the SO_2 molecules could diffuse inside the aggregates, through the channels. Thus, the chemisorption may take place on the basic and redox active sites of the intra-aggregates surface. Moreover, the third sulfur species, according to the doublet in the S 2p spectra located at B.E. S $2p_{3/2}$ = 170.5eV, could be explained by the formation of a multilayer adsorption of trapped SO_2 molecules resulting of their diffusion in the channels (Figure 6). As a result,

sulfur atoms of these trapped gaseous probe molecules may have interactions with second neighbor oxygen atoms, which impacts the electronic structure of sulfur atoms and therefore their B.E., resulting in the appearance of this new higher binding energy component[50].

These hypotheses were confirmed by exposing the samples to SO_2 Pulses Chemisorption Analysis. This experiment makes it possible to send a well-defined quantity of SO_2 (0.5 cc of reactive gas) and follow the SO_2 consumption by the material. In pulse chemisorption experiment, the exposure time is very short which limits the gaseous probes diffusion inside the aggregates. The surface saturation has been reached after 45 pulses of 5% SO_2/He. The sample was then analyzed by XPS. We determined that the S/Co ratio value reaches 0.28. This ratio fits well with the S/Co ratio value of the plateau (step 2). We can thus confirm that the step 2 is related to the saturation of the surface of the aggregates.
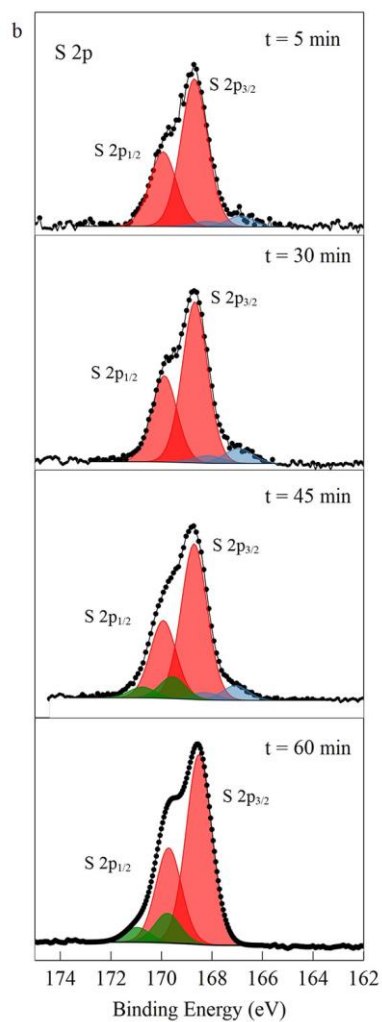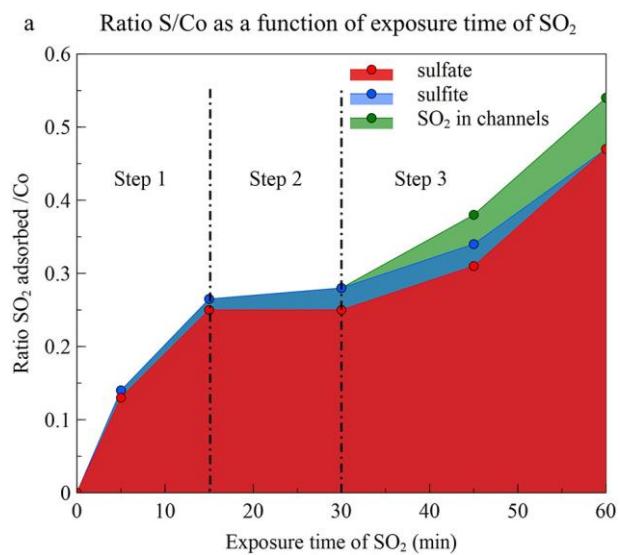
Figure 5: a) Ratio SO$_2$ adsorbed/Co, b) S 2p core peaks for an exposure at the SO$_2$ flow during 5, 30, 45 and 60 min.
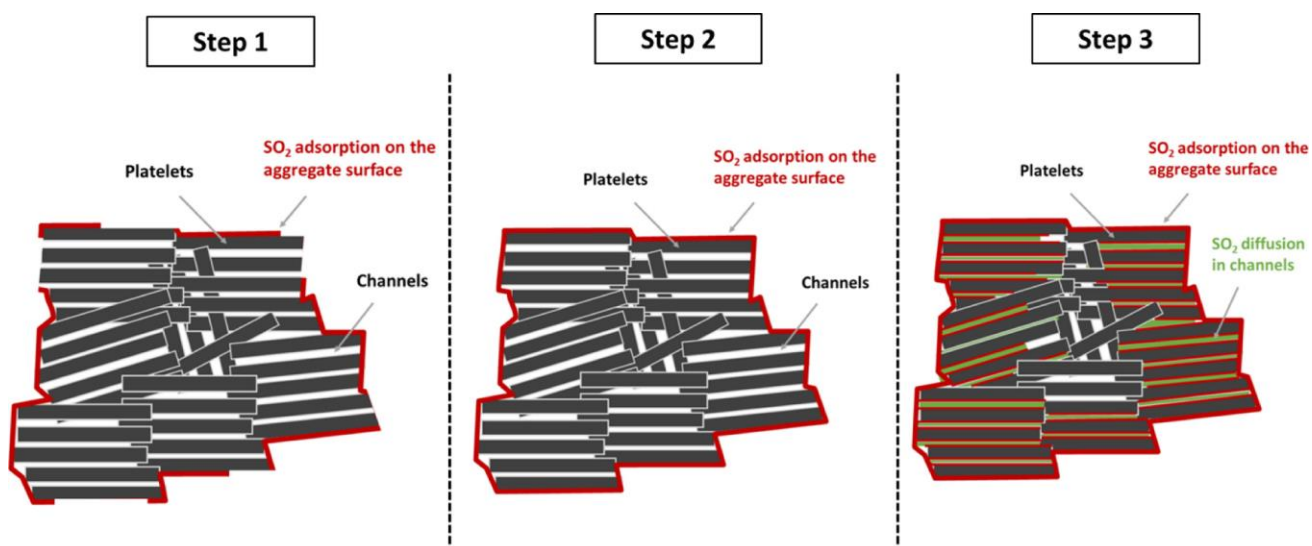
Figure 6: Schematic view of a β(III)-CoOOH aggregate upon adsorption.

2) *Modelling of SO₂ adsorption*

The adsorption of the gas probe was investigated from a computational approach by adsorbing a SO_2 molecule on the top atomic layer of the (001), (012) and (110) slab models. We considered the adsorption of the SO_2 molecule on top of an oxygen atom, corresponding to the formation of sulfite species, and in a bridge configuration, between two oxygen atoms, corresponding to the formation of a sulfate species. To avoid periodic image interactions between SO_2 molecules, we followed a supercell approach and slab with an in-plane length of about 10 Å were built. This leads to a low coverage of the surface, the S/Co ratio being around 3%, with a weak interaction between SO_2 molecule and its periodic image. Then the positions of all atoms were relaxed to compute the adsorption energies. The electronic charge transfer from the SO_2 molecule toward the slab was computed using the Bader's charges.

The computed adsorption energies and the charge transfer after SO_2 adsorption are presented in Table 3. On the (001) surface, the formation of sulfate species is an endothermic reaction while sulfite species appear to be unstable. On the (012) and the (110) surfaces, the adsorption of both sulfite and sulfate species is an exothermic reaction. In agreement with previous works[13,35], the formation of sulfate

species is accompanied by a charge transfer of about 1.1 to 1.2e toward the surface, associated to a redox reaction, while a low charge transfer from the surface is obtained in the case of the formation of sulfite species.

On both (012) and (110) surfaces, the formation of sulfate species is favored. However, on the (012) surface, the adsorption energies rather correspond to week interactions and might not be strong enough to be detected by XPS with ultra-vacuum conditions. On the contrary, on the (110) surface, the adsorption energies correspond to chemisorption. These results let us assume that the reactivity of β(III)-CoOOH material is determined by the presence on the surface of undercoordinated cobalt atoms in Co^{4+} oxidation degrees. Indeed, the active sites on (001) or (012) surfaces, which exhibit Co^{3+} species, lead to a weak reactivity or the absence of reactivity while the (110) surface, with Co^{4+} species, leads to strong adsorptions. As a consequence, we will focus on the adsorptions on the (110) surface and analyze the electronic processes taking place when an SO_2 adsorption occurs. The electronic configuration of cobalt atoms and the top and side view of the system after SO_2 adsorption are depicted in Figure 7 for sulfite and sulfate adsorption.

In the case of the sulfate adsorption, the magnetic moments of the two cobalt atoms bonded to the adsorption site (cobalt atoms surrounded in orange in Figure 7.a) decrease from $2.95\mu_B$ to $2.67\mu_B$, while the atomic charges decrease from 1.43 to 1.27e and the total number of unpaired electrons decreases by an amount of 2 electrons. These results agree with the transfer of formally two electrons from the SO_2 molecule to the slab and the reduction of the two cobalt atoms from Co^{4+} to Co^{3+} species with an intermediary spin configuration, the electrons coming from SO_2, completing the t_{2g} states of the cobalt atoms, see Figure 7a. According to our reference calculations, Figure SI-13 in the supporting information, the magnetic moment and the charge of the cobalt atoms agree with a Co^{3+} species. Moreover, a secondary interaction between an adsorbed oxygen and a surface cobalt atom is present due to the orientation of the molecule towards the surface. This interaction completes the coordination

sphere of the cobalt with a bond length of 2.21 Å, knowing that the Co-O bond lengths in the bulk are 1.90 Å.

In the case of the formation of sulfite species, Figure 7.b, the SO_2 molecule is bonded to one oxygen atom and stabilized by interactions between the two oxygen atoms of SO_2 and one cobalt atom and one hydrogen atom of the surface. The bond length between the oxygen atom of SO_2 and the hydrogen atom of the surface is 2.45 Å corresponding to a weak interaction. The bond length between the cobalt atom of the surface layer and the oxygen atom of SO_2 is 2.04 Å. This is close to the Co-O bond length in the bulk and thus completes the coordination sphere of this cobalt atom. The final environment of this cobalt atom is thus ML_5 and its magnetic moment decreases from $2.95\mu_B$ to $1.88\mu_B$ while its charge decreases from 1.43e to 1.38e. These results are really close to the previous calculations on the (012) slab model with cobalt atom in a ML_5 environment, see Figure 4.b, and correspond to Co^{3+} species. Contrary to the case of the sulfate species formation, in this case, the reduction of the Co^{4+} is not associated to the oxidation of the sulfur atom of SO_2 but to an interaction between one lone pair of an oxygen atom from the SO_2 molecule and the surface. As a consequence, from the point of view of the probe, it is not a redox process because no electron transfer takes place.
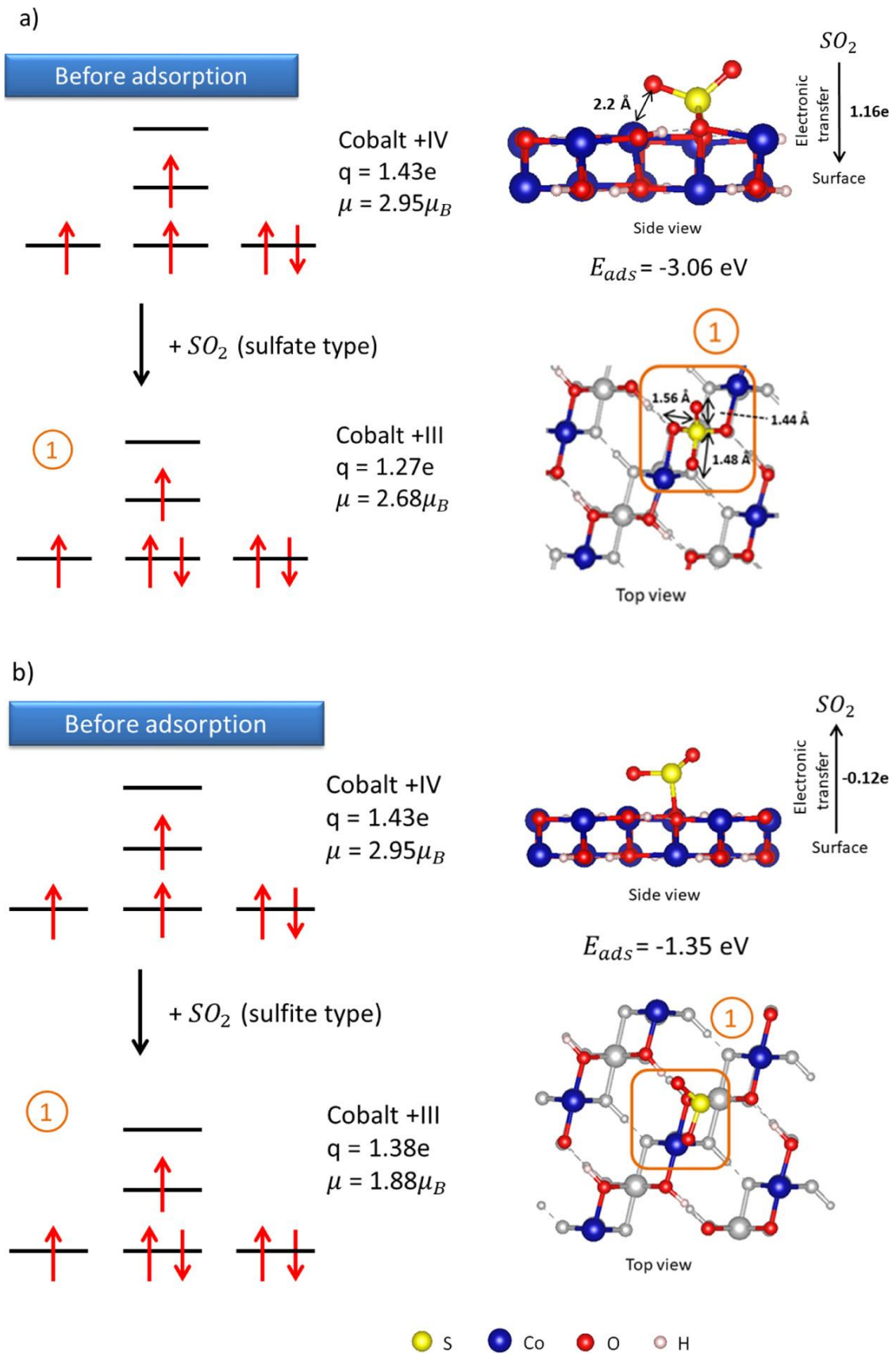
Figure 7: (a) Sulfate and (b) sulfite adsorption modes

on (110)-surface of β(III)-CoOOH

Table 3: Adsorption energy and electronic transfer on surfaces (001), (110) and (012) of β(III)-CoOOH

Surface	species	E_{ads} (eV)	Δq SO_2
(001)	sulfate	0.68	1.12
(001)	sulfite	No adsorption on the surface	
(110)	Sulfate	-3.06	1.16
(110)	Sulfite	-1.35	-0.12
(012)	Sulfate	-0.95	1.12
(012)	Sulfite	-0.14	-0.11

To conclude on the adsorption of SO_2 on the β(III)-CoOOH material, we showed that the formation of sulfate species is favored while sulfite species are obtained in a lesser extent. Three slab models were investigated in the computational approach in order to consider different local environments of the cobalt atom on the atomic surface layer. These local environments and the associated cobalt species are the key factor of the surface reactivity and correspond to a microscopic view of the overall electrochemical behavior. The reactivity of the surface is mainly associated to a redox mechanism and depends on the environment and the oxidation degrees of the cobalt surface atoms. ML_6 and ML_5 environments associated to Co^{3+} species lead to a weak or an absence of reactivity. On the contrary, the presence of ML_4 environment with Co^{4+} species leads to strong chemisorption and redox mechanism. This kind of redox reactivity agrees with the pseudo-capacitive behavior of β(III)-CoOOH electrode material and we showed that it is linked to undercoordinated cobalt species with high oxidation degrees, namely Co^{4+}. Moreover, these species might be available at the surface of the particle aggregates or inside the channels between aggregates. In order to enhance the redox reactions involved in pseudocapacitive processes, such Co^{4+} species should be favored in the synthesis of electrode materials, either via the growth of particles with a specific morphology (rods) exhibiting a

large amount of surface such as the (110) surface associated to the cleavage or two Co-O bonds (ML$_4$ environment) or the presence of defects leading to the formation of Co^{4+} species on top of more likely surfaces such as the (001) surface.

IV) Conclusion

The aim of this work was to investigate the surface reactivity of the β(III)-CoOOH materials from both experimental and computational approaches. Adsorption of gaseous probe molecules (SO$_2$) followed by XPS analyses were implemented in parallel with DFT+U periodic calculations of the bulk and several surfaces of the β(III)-CoOOH materials.

We showed that the synthesis of the material leads to the formation of disordered aggregates of β(III)-CoOOH small platelets of length 60-100nm. The cobalt atoms at the surface are Co^{3+} species with a small amount of Co^{4+} species (1-6%). The disordered morphology of the aggregates leads to a kinetics of the SO$_2$ adsorption that takes place in three steps. The first step consists in the adsorption around the aggregates, followed by a latency period preceding the last step corresponding to the adsorption of SO$_2$ molecules in the channels inside the aggregates. From XPS analysis, we observed that sulfate species (redox sites) are favored at the surface of the aggregates and inside the channels while sulfite species (basic sites) are observed in a lesser extent. From the surface and adsorption calculations, we conclude that the reactivity of the surface is associated to the presence of undercoordinated ML$_4$ Co^{4+} species. Such Co^{4+} cobalt species might be obtained either through a specific morphology of the material (rods) that leads to an important proportion of surface such as the (110) surface associated to the cleavage or two Co-O bonds, or from the formation of defects on top of more likely surfaces such as the (001) one.

This points out the structural characteristics for which we could expect to optimize the surface reactivity of β(III)-CoOOH. Therefore, it appears that the development of material with [110] growing

direction or a large proportion of surface defects should enhance the adsorption capacity and thus increase the electrochemical performances.

Supporting Information.

The supporting information provides: complementary XPS results; complementary data on cobalt oxides bulk and surfaces from DFT calculations.

Acknowledgement

References:

1. Simon, P.; Gogotsi, Y. Materials for electrochemical capacitors. *Nat. Mater.* **2008**, *7*, 845– 854, DOI: 10.1038/nmat2297
2. Choudhary, N.; Li, C.; Moore, J.; Nagaiah, N.; Zhai, L.; Jung, Y.; Thomas, J. Asymmetric Supercapacitor Electrodes and Devices. *Adv. Mater.* **2017**, *29*, 1605336, DOI: 10.1002/adma.201605336
3. Shao, Y.; El-Kady, M. F.; Sun, J.; Li, Y.; Zhang, Q.; Zhu, M.; Wang, H.; Dunn, B.; Kaner, R. B. Design and Mechanisms of Asymmetric Supercapacitors. *Chem. Rev.* **2018**, *118*, 9233– 9280, DOI: 10.1021/acs.chemrev.8b00252
4. Lin, Z.; Goikolea, E.; Balducci, A.; Naoi, K.; Taberna, P. L.; Salanne, M.; Yushin, G.; Simon, P. Materials for Supercapacitors: When Li-Ion Battery Power Is Not Enough. *Mater. Today* **2018**, *21*, 419– 436, DOI: 10.1016/j.mattod.2018.01.035
5. Nguyen, T.; Montemor, M. d. F. Metal Oxide and Hydroxide–Based Aqueous Supercapacitors: From Charge Storage Mechanisms and Functional Electrode Engineering to Need-Tailored Devices. *Adv. Sci.* **2019**, *6*, 1801797, DOI: 10.1002/advs.201801797
6. Jiang, Y.; Liu, J. Definitions of Pseudocapacitive Materials: A Brief Review. *Energy Environ. Mater.* **2019**, *2*, 30– 37, DOI: 10.1002/eem2.12028
7. Brousse, T.; Bélanger, D.; Long, J. W. To Be or Not To Be Pseudocapacitive?. *J. Electrochem. Soc.* **2015**, *162*, A5185– A5189, DOI: 10.1149/2.0201505jes
8. Tang, C.; Giaume, D.; Weill, F.; Penin, N.; Dourges, M.-A.; Saadaoui, H.; Guerlou-Demourgues, L. Synergy of Mn and Co in Slab-Based Nanocomposites for Hybrid Supercapacitors: Impact of Restacking Process on Electrochemical Properties. *ACS Appl. Energy Mater.* **2019**, *2*, 7832– 7842, DOI: 10.1021/acsaem.9b01263
9. Xia, H.; Shirley Meng, Y.; Yuan, G.; Cui, C.; Lu, L. A Symmetric RuO2/RuO2 Supercapacitor Operating at 1.6 V by Using a Neutral Aqueous Electrolyte. *Electrochem. Solid-State Lett.* **2012**, *15*, A60, DOI: 10.1149/2.023204esl

10. Lukatskaya, M. R.; Mashtalir, O.; Ren, C. E.; Dall'Agnese, Y.; Rozier, P.; Taberna, P. L.; Naguib, M.; Simon, P.; Barsoum, M. W.; Gogotsi, Y. Cation Intercalation and High Volumetric Capacitance of Two-Dimensional Titanium Carbide. *Science* **2013**, *341*, 1502– 1505, DOI: 10.1126/science.1241488

11. Brousse, T.; Toupin, M.; Dugas, R.; Athouël, L.; Crosnier, O.; Bélanger, D. Crystalline MnO_2 as Possible Alternatives to Amorphous Compounds in Electrochemical Supercapacitors. *J. Electrochem. Soc.* **2006**, *153*, A2171, DOI: 10.1149/1.2352197

12. Olchowka, J.; Tailliez, T.; Bourgeois, L.; Dourges, M. A.; Guerlou-Demourgues, L. Ionic Liquids to Monitor the Nano-Structuration and the Surface Functionalization of Material Electrodes: A Proof of Concept Applied to Cobalt Oxyhydroxide. *Nanoscale Adv.* **2019**, *1*, 2240– 2249, DOI: 10.1039/c9na00171a

13. Andreu, N.; Baraille, I.; Martinez, H.; Dedryvère, R.; Loudet, M.; Gonbeau, D. New Investigations on the Surface Reactivity of Layered Lithium Oxides. *J. Phys. Chem. C* **2012**, *116*, 20332– 20341, DOI: 10.1021/jp304293u

14. Quesne-Turin, A.; Vallverdu, G.; Flahaut, D.; Allouche, J.; Croguennec, L.; Ménétrier, M.; Baraille, I. Morphology and Surface Reactivity Relationship in the Li1+xMn2–XO4 Spinel with x = 0.05 and 0.10: A Combined First-Principle and Experimental Study. *ACS Appl. Mater. Interfaces* **2017**, *9*, 44922– 44930, DOI: 10.1021/acsami.7b15249

15. Quesne-Turin, A.; Flahaut, D.; Croguennec, L.; Vallverdu, G.; Allouche, J.; Charles-Blin, Y.; Chotard, J.-N.; Ménétrier, M.; Baraille, I. Surface Reactivity of Li2MnO3: First-Principles and Experimental Study. *ACS Appl. Mater. Interfaces* **2017**, *9*, 44222– 44230, DOI: 10.1021/acsami.7b14826

16. Tang, C.; Giaume, D.; Guerlou-Demourgues, L.; Lefèvre, G.; Barboux, P. Prediction of Isoelectric Point of Manganese and Cobalt Lamellar Oxides: Application to Controlled Synthesis of Mixed Oxides. *Langmuir* **2018**, *34*, 6670– 6677, DOI: 10.1021/acs.langmuir.8b00190

17. Butel, M.; Gautier, L.; Delmas, C. Cobalt oxyhydroxides obtained by "chimie douce" reactions: structure and electronic conductivity properties. *Solid State Ionics* **1999**, *122*, 271– 284, DOI: 10.1016/s0167-2738(99)00076-4

18. Lee, K. K.; Chin, W. S.; Sow, C. H. Cobalt-Based Compounds and Composites as Electrode Materials for High-Performance Electrochemical Capacitors. *J. Mater. Chem. A* **2014**, *2*, 17212– 17248, DOI: 10.1039/c4ta02074j

19. Wen, W.; Liang, D.; Cheng, J.-P.; Wu, J.-M. CoOOH Ultrafine Nanoparticles for Supercapacitors. *RSC Adv.* **2016**, *6*, 70947– 70951, DOI: 10.1039/c6ra14347d

20. Scofield, J. H. Hartree-Slater subshell photoionization cross-sections at 1254 and 1487eV. *J. Electron. Spectrosc. Relat. Phenom.* **1976**, *8*, 129– 137, DOI: 10.1016/0368-2048(76)80015-1

21. Andreu, N.; Flahaut, D.; Dedryvère, R.; Minvielle, M.; Martinez, H.; Gonbeau, D. XPS Investigation of Surface Reactivity of Electrode Materials: Effect of the Transition Metal. *ACS Appl. Mater. Interfaces* **2015**, *7*, 6629– 6636, DOI: 10.1021/am5089764

22. Guimon, C.; Gervasini, A.; Auroux, A. XPS Study of the Adsorption of SO 2 and NH 3 over Supported Tin Dioxide Catalysts Used in de-NOx Catalytic Reaction. *J. Phys. Chem. B* **2001**, *105*, 10316– 10325, DOI: 10.1021/jp0108869

23. Kresse, G.; Hafner, J. Ab Initio Molecular-Dynamics Simulation of the Liquid-Metal–Amorphous-Semiconductor Transition in Germanium. *Phys. Rev. B: Condens. Matter Mater. Phys.* **1994**, *49*, 14251– 14269, DOI: 10.1103/physrevb.49.14251

24. Kresse, G.; Furthmüller, J. Efficient Iterative Schemes for Ab Initio Total-Energy Calculations Using a Plane-Wave Basis Set. *Phys. Rev. B: Condens. Matter Mater. Phys.* **1996**, *54*, 11169– 11186, DOI: 10.1103/physrevb.54.11169

25. Kresse, G.; Joubert, D. From Ultrasoft Pseudopotentials to the Projector Augmented-Wave Method. *Phys. Rev. B: Condens. Matter Mater. Phys.* **1999**, *59* (3), 1758– 1775, DOI: 10.1103/PhysRevB.59.1758

26. Perdew, J. P.; Burke, K.; Ernzerhof, M. Generalized Gradient Approximation Made Simple. *Phys. Rev. Lett.* **1996**, *77* (18), 3865– 3868, DOI: 10.1103/PhysRevLett.77.3865

27. Chen, Z.; Kronawitter, C. X.; Yeh, Y.-W.; Yang, X.; Zhao, P.; Yao, N.; Koel, B. E. Activity of Pure and Transition Metal-Modified CoOOH for the Oxygen Evolution Reaction in an Alkaline Medium. *J. Mater. Chem. A* **2017**, *5*, 842– 850, DOI: 10.1039/c6ta07482k

28. Dudarev, S. L.; Botton, G. A.; Savrasov, S. Y.; Humphreys, C. J.; Sutton, A. P. Electron-energy-loss spectra and the structural stability of nickel oxide: An LSDA+U study. *Phys. Rev. B: Condens. Matter Mater. Phys.* **1998**, *57*, 1505– 1509, DOI: 10.1103/physrevb.57.1505

29. Kramer, D.; Ceder, G. Tailoring the Morphology of LiCoO2: A First Principles Study. *Chem. Mater.* **2009**, *21* (16), 3799– 3809, DOI: 10.1021/cm9008943

30. Dahéron, L.; Dedryvère, R.; Martinez, H.; Ménétrier, M.; Denage, C.; Delmas, C.; Gonbeau, D. Electron Transfer Mechanisms upon Lithium Deintercalation from LiCoO 2 to CoO 2 Investigated by XPS. *Chem. Mater.* **2008**, *20*, 583– 590, DOI: 10.1021/cm702546s

31. Yang, J.; Liu, H.; Martens, W. N.; Frost, R. L. Synthesis and Characterization of Cobalt Hydroxide, Cobalt Oxyhydroxide, and Cobalt Oxide Nanodiscs. *J. Phys. Chem. C* **2010**, *114*, 111– 119, DOI: 10.1021/jp908548f

32. Tasker, P. W. The Stability of Ionic Crystal Surfaces. *J. Phys. C: Solid State Phys.* **1979**, *12* (22), 4977, DOI: 10.1088/0022-3719/12/22/036

33. Tang, W; Sanville, E; Henkelman, G A Grid-Based Bader Analysis Algorithm without Lattice Bias. *J. Phys.:*

34. Henkelman, G.; Arnaldsson, A.; Jonsson, H. A Fast and Robust Algorithm for Bader Decomposition of Charge Density.. *Comput. Mater. Sci.* **2006**, *36* (3), 354– 360, DOI: 10.1016/j.commatsci.2005.04.010

35. Vallverdu, G.; Minvielle, M.; Andreu, N.; Gonbeau, D.; Baraille, I. First Principle Study of the Surface Reactivity of Layered Lithium Oxides LiMO2 (M = Ni, Mn, Co). *Surf. Sci.* **2016**, *649*, 46– 55, DOI: 10.1016/j.susc.2016.01.004

36. Chen, J.; Selloni, A. First Principles Study of Cobalt (Hydr)Oxides under Electrochemical Conditions. *J. Phys. Chem. C* **2013**, *117*, 20002– 20006, DOI: 10.1021/jp406331h

37. Chen, Z.; Kronawitter, C. X.; Waluyo, I.; Koel, B. E. Investigation of Water Dissociation and Surface Hydroxyl Stability on Pure and Ni-Modified CoOOH by Ambient Pressure Photoelectron Spectroscopy. *J. Phys. Chem. B* **2018**, *122*, 810– 817, DOI: 10.1021/acs.jpcb.7b06960

38. Scherrer, P. Determination of the size and internal structure of colloidal particles using X-rays. *Nachr. Ges. Wiss. Göttingen, Math-Phys. Kl* **1918**, 98– 100.

39. Tang, C. Exfoliation et réempilement d'oxydes lamellaires à base de manganese et de cobalt pour electrodes de supercondensateurs. Ph.D. Dissertation, Université de Bordeaux, Bordeaux, 2017.

40. Zhang, D.; Kong, X.; Zhao, Y.; Jiang, M.; Lei, X. CoOOH Ultrathin Nanoflake Arrays Aligned on Nickel Foam: Fabrication and Use in High-Performance Supercapacitor Devices. *J. Mater. Chem. A* **2016**, *4*, 12833– 12840, DOI: 10.1039/c6ta04413a

41. Justin Raj, C.; Kim, B. C.; Cho, W.-J.; Park, S.; Jeong, H. T.; Yoo, K.; Yu, K. H. Rapid Hydrothermal Synthesis of Cobalt Oxyhydroxide Nanorods for Supercapacitor Applications. *J. Electroanal. Chem.* **2015**, *747*, 130– 135, DOI: 10.1016/j.jelechem.2015.04.013

42. Liao, D.-q.; Xi, X.-m. Study on the preparation of LiCoO2 by multiphase redox method. *Powder Technol.* **2014**, *253*, 146– 151, DOI: 10.1016/j.powtec.2013.11.012

43. Zhen-Yu, L. Improvement in the surface properties of activated carbon via steam pretreatment for high performance supercapacitors. *Appl. Surf. Sci.* **2017**, *404*, 88– 93, DOI: 10.1016/j.apsusc.2017.01.238

44. El-Kady, M. F.; Strong, V.; Dubin, S.; Kaner, R. B. Laser Scribing of High-Performance and Flexible Graphene-Based Electrochemical Capacitors. *Science* **2012**, *335*, 1326– 1330, DOI: 10.1126/science.1216744

45. Dedryvère, R.; Laruelle, S.; Grugeon, S.; Poizot, P.; Gonbeau, D.; Tarascon, J.-M. Contribution of X-ray Photoelectron Spectroscopy to the Study of the Electrochemical Reactivity of CoO toward Lithium. *Chem. Mater.* **2004**, *16*, 1056– 1061, DOI: 10.1021/cm0311269

46. Kim, K. S. X-ray-photoelectron spectroscopic studies of the electronic structure of CoO. *Phys. Rev. B: Solid State* **1975**, *11*, 2177– 2185, DOI: 10.1103/physrevb.11.2177

47. Godillot, G.; Guerlou-Demourgues, L.; Taberna, P.-L.; Simon, P.; Delmas, C. Original conductive nano-Co_3O_4 investigated as electrode material for hybrid supercapacitor. *Electrochem. Solid-State Lett.* **2011**, *14*, A139, DOI: 10.1149/1.3609259

48. Shaju, K. M.; Guerlou-Demourgues, L.; Godillot, G.; Weill, F.; Delmas, C. Strategies for Synthesizing Conductive Spinel Cobalt Oxide Nanoparticles for Energy Storage Applications. *J. Electrochem. Soc.* **2012**, *159*, A1934, DOI: 10.1149/2.036212jes

49. Godillot, G.; Guerlou-Demourgues, L.; Croguennec, L.; Shaju, K. M.; Delmas, C. Effect of Temperature on Structure and Electronic Properties of Nanometric Spinel-type Cobalt Oxides. *J. Phys. Chem. C* **2013**, *117*, 9065– 9075, DOI: 10.1021/jp3100359

50. Lindberg, B. J.; Hamrin, K.; Johansson, G.; Gelius, U.; Fahlman, A.; Nordling, C.; Siegbahn, K. Molecular Spectroscopy by Means of ESCA II. Sulfur compounds. Correlation of electron binding energy with structure. *Phys. Scr.* **1970**, *1*, 286– 298, DOI: 10.1088/0031-8949/1/5-6/020

TOC Graphic